

Cite this: *J. Mater. Chem. A*, 2021, 9, 5815

A thermally robust and strongly oxidizing surface of WO₃ hydrate nanowires for electrical aldehyde sensing with long-term stability†

Guozhu Zhang,^{ab} Takuro Hosomi,^{ac} Wataru Mizukami,^{cde} Jianguang Liu,^{ab} Kazuki Nagashima,^{ac} Tsunaki Takahashi,^{ac} Masaki Kanai,^{ab} Takeharu Sugiyama,^f Takao Yasui,^{cg} Yuriko Aoki,^b Yoshinobu Baba,^g Johnny C. Ho,^{bh} and Takeshi Yanagida^{ab*}

Electrical molecular nanosensors require two conflicting surface characteristics, which are catalytic activity for molecular selectivity and thermal stability for long-term data collection. Here, we show that a simple surface treatment using strong acids creates two such conflicting surface properties of WO₃ hydrate nanowires, which enhance the electrical molecular sensing of aldehydes (nonanal, a biomarker). Mass-spectrometric measurements reveal that the surface treatment using strong acids substantially promotes both the oxidization of nonanal and the desorption of products, nonanoic acid, from the surfaces at a temperature of 50 °C, which is lower than the 300 °C required for untreated surfaces. Spectroscopic and structural measurements combined with numerical simulations identify two different adsorption structures of carbonyl groups on the surface, where molecules directly bound to coordinatively unsaturated surface tungsten preferentially proceed to the catalytic oxidization reaction and the subsequent desorption process. Furthermore, we confirm the thermal durability (over 10 years) of the catalytic activity on acid-treated WO₃ hydrate nanowire surfaces up to 300 °C, which enables us to demonstrate the long-term stable sensor operations with the sensitivity (4 orders of magnitude) remaining for years.

Received 19th November 2020

Accepted 26th January 2021

DOI: 10.1039/d0ta11287a

rsc.li/materials-a

Introduction

Electrical molecular sensing of various chemical species has been recently offering new scientific and industrial approaches to understand inherently complex systems (biological activity, chemical processing, human metabolism and others) *via*

analyzing the collected chemical big-data, which can be further combined with the available existing data obtained using physical sensors.^{1–5} Among various molecular sensing methods, heterogeneous catalysis-based molecular sensing is particularly promising for such electrical molecular sensing devices for long-term data collection.^{6–8} This is because such heterogeneous catalysis on solid surfaces enables molecular transformations with electron transfer,⁹ which essentially enhance the molecular sensitivity and selectivity in recorded electrical signals.^{9–11} To improve heterogeneous catalysis-based electrical molecular sensing, there are inherently two requirements, which are catalytic activity for molecular selectivity and thermal robustness for long-term data collection.^{12–14} Because in general catalytic activity tends to deactivate over time, especially when sensing in a high temperature range.^{15,16} This would greatly limit the practical applications of such kinds of molecular sensors for trace molecule (ppb to ppt level) detection and discrimination, for example, trace nonanal (aldehyde, a lung cancer biomarker) detection from exhaled breath for lung cancer early screening and diagnosis.¹⁷ Thus, satisfying both requirements of catalytic activity and thermal robustness on sensor surfaces is essential to design long-term stable molecular nanosensors using catalysis.

^aDepartment of Applied Chemistry, Graduate School of Engineering, The University of Tokyo, 7-3-1, Hongo, Bunkyo-ku, Tokyo, 113-8654, Japan. E-mail: yanagida@g.ecc.u-tokyo.ac.jp

^bInstitute for Materials Chemistry and Engineering, Kyushu University, 6-1 Kasuga-Koen, Kasuga, Fukuoka, 816-8580, Japan

^cJST-PRESTO, 4-1-8 Honcho, Kawaguchi, Saitama 332-0012, Japan

^dCenter for Quantum Information and Quantum Biology, Institute for Open and Transdisciplinary Research Initiatives, Osaka University, Osaka 560-8531, Japan

^eGraduate School of Engineering Science, Osaka University, 1-3 Machikaneyama, Toyonaka, Osaka 560-8531, Japan

^fResearch Center for Synchrotron Light Applications, Kyushu University, 6-1 Kasuga-koen, Kasuga, Fukuoka 816-8580, Japan

^gGraduate School of Engineering, Nagoya University, Furo-cho, Chikusa-ku, Nagoya 464-8603, Japan

^hDepartment of Materials Science and Engineering, State Key Laboratory of Terahertz and Millimeter Waves, Centre for Functional Photonics, City University of Hong Kong, Kowloon 999077, Hong Kong SAR

† Electronic supplementary information (ESI) available. See DOI: 10.1039/d0ta11287a

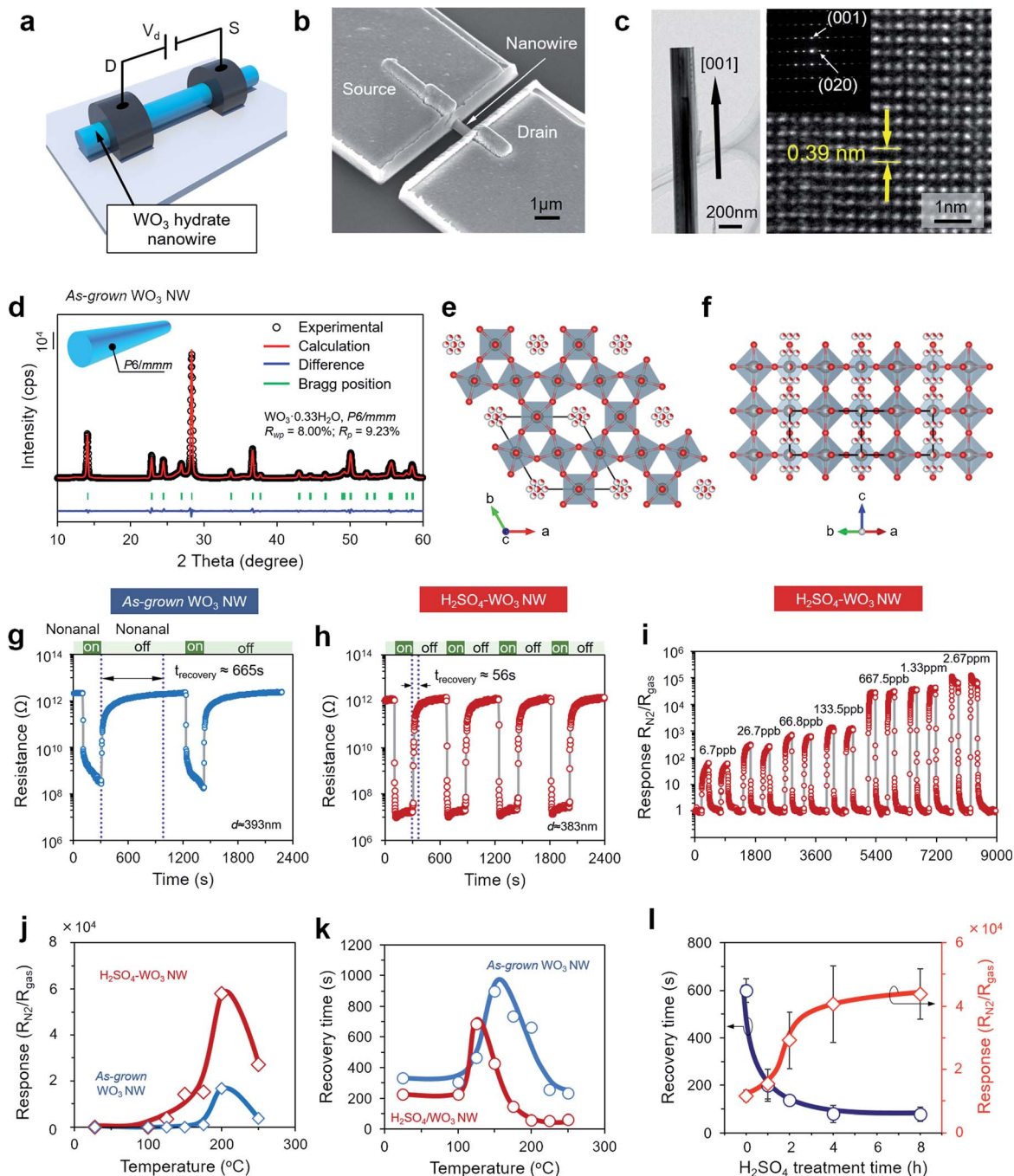


Fig. 1 (a) Schematic illustration and (b) SEM image of a single WO_3 hydrate nanowire sensor device. (c) Transmission electron microscopy (TEM) and selected area electron diffraction (SAED) images of a WO_3 hydrate nanowire. (d) X-ray diffraction (XRD) pattern and the Rietveld refinement of the as-grown WO_3 hydrate nanowires. Projections of the as-grown WO_3 hydrate nanowires along the (e) c axis and (f) the $[110]$ direction. The red sectors in water "dots" represent the probability of water's presence at the corresponding sites. (g) and (h) show the sensor response data of both as-grown and H_2SO_4 -surface treated WO_3 hydrate nanowire sensors when introducing 2.67 ppm nonanal at 200 °C. Recovery time is defined as the time required to obtain the 90% original resistance value. (i) Dynamic resistance response of the H_2SO_4 -surface treated WO_3 nanowire sensor device to various concentrations (from 6.7 ppb to 2.67 ppm) of nonanal at 200 °C (Fig. S2†). (j) and (k) show the temperature-dependent sensing response and recovery time of the as-grown and H_2SO_4 -surface treated WO_3 nanowire sensor devices to 2.67 ppm nonanal (Fig. S3†). (l) Recovery time and sensing response of the WO_3 hydrate single nanowire device at 200 °C when varying the surface acid treatment time (Fig. S5†).

To fulfill these two requirements, previous studies on heterogeneous catalysis-based electrical molecular sensing have utilized various nanostructures, including thermally robust

metal oxides,^{18,19} noble metal nanostructures supported on metal oxides^{20–22} and heterostructures.^{23–25} For example, nanostructured metal oxides have been tailored by intentionally

introducing oxygen vacancies to enhance the catalysis for electrical molecular sensing.^{26–28} Noble metal nanostructures on metal oxide surfaces exhibit the so-called spillover effects for gas molecules, which enhance the catalysis and the electrical molecular sensing.^{20,29,30} Heterostructures are also promising candidates to enhance catalysis-based electrical molecular sensing *via* the presence of a hetero-interface, where a built-in electrical potential exists.^{7,23–25} Although these nanostructures are practically useful for heterogeneous catalysis-based molecular sensing, designing and tailoring of long-term stable catalysts for molecular sensing are still based on a rule of thumb mainly due to the lack of knowledge as to complex molecular transformation behavior on nanostructured catalyst surfaces and the correlation between molecular behavior, surface structures and recorded electrical signals.^{21–30} For these reasons, various *operando* methodologies, including diffuse reflectance infrared Fourier transform spectroscopy (DRIFT), Raman, UV/Vis, X-ray absorption spectroscopy and X-ray diffraction, have been introduced to understand the mechanisms of heterogeneous catalysis-based electrical molecular sensing.^{31–35} For example, the *operando* DRIFT method is a powerful technique for on-line analysis of molecular reaction products on the sensor surface.^{31,36–39} These *operando* techniques frequently sacrifice their sensitivity and resolution for *in situ* operations.^{31,36–39} We have recently reported a methodology to monitor surface molecular transformation behavior, which is sensitive enough even for relatively low-density molecules adsorbed on nanostructured oxides, using a combined technique of infrared *p*-polarized multiple-angle incidence resolution spectroscopy and temperature programmed desorption/gas chromatography mass spectrometry.⁴⁰

In this study, we demonstrate thermally robust and catalytically active sensor surfaces of WO₃ hydrate nanowires for electrical aldehyde (nonanal) sensing by monitoring their surface molecular transformation behavior under sensing environments. Mass-spectrometric, spectroscopic and structural measurements combined with numerical simulations reveal the presence of thermally robust and coordinatively unsaturated tungstens on WO₃ hydrate nanowire surfaces.

Results and discussion

First, we show the effect of surface treatment using sulfuric acid (H₂SO₄) on the electrical response data of the WO₃ hydrate nanowire sensor. Fig. 1a and b show the schematic image and scanning electron microscopy image (SEM) of the fabricated sensor device composed of a single WO₃ hydrate nanowire and Pt electrodes. The transmission electron microscopy (TEM) and selected area electron diffraction (SAED) images of the fabricated WO₃ hydrate nanowires are shown in Fig. 1c, revealing that the as-grown nanowire is a single crystalline hexagonal crystal structure and the growth direction can be assigned to [001]. Fig. 1d shows the XRD data, which reveal the WO₃ hydrate crystal structure (WO₃·*n*H₂O), as illustrated in Fig. 1e and f. In the single nanowire sensor device, the open-top gap between electrodes was designed to be 1 μm. The details of sensor device fabrication processes can be seen in the Experimental section.

We performed a surface treatment of the as-grown WO₃ hydrate nanowires using sulfuric acid (H₂SO₄ conc.) for 4 h (Fig. S1,† SEM data). Fig. 1g and h show the comparison between (1) the sensor device composed of the as-grown WO₃ nanowires and (2) the sensor device composed of the H₂SO₄-surface treated WO₃ nanowires with respect to the electrical response data when introducing 2.67 ppm nonanal. The operating temperature was 200 °C. As can be seen, the surface treatment significantly enhances the sensor electrical response and the recovery rate. We confirm this significant effect of surface acid treatment on both the nonanal concentration dependence data (Fig. 1i) and the operating temperature dependence data (Fig. 1j and k). The acid surface treated sensor device exhibits a detectable electrical response down to 6.7 ppb, which is two times lower than that of the as-grown WO₃ hydrate nanowire sensor (13.4, Fig. S2†). Note that the observed nonanal sensing performance of the acid surface treated WO₃ nanowire sensor device is superior in sensitivity and ultralow in the detection limit to that of previously reported nonanal sensors as summarized in ESI Table S1.† In addition, molecular sensing selectivity evaluation showed that the acid surface treated sensor presents selectivity to nonanal (Fig. S4†). To further confirm the effect of surface acid treatment, the surface treatment time dependence of the sensor properties (sensor response ratio and recovery time data) are shown in Fig. 1l. Clearly, increasing the surface acid treatment time improves the sensor properties (*i.e.* increasing the sensor response and decreasing the sensor recovery time). Thus, the simple surface treatment using H₂SO₄ significantly improves the electrical response behavior of WO₃ hydrate nanowire sensors.

Since the observed electrical response in Fig. 1 is inherently determined by the surface chemical reaction events, we performed temperature-programmed desorption/gas chromatography mass spectrometry (TPD-GCMS) to analyze the chemical compositions of the desorbed molecules from nonanal-adsorbed WO₃ hydrate nanowire surfaces, as shown in Fig. 2a and b. The temperature-dependent chromatograms show that not only nonanal (retention time, 19.8 min, Fig. S7†) but also nonanoic acid (retention time, 31.1 min, Fig. S7†) is included in the desorbed molecules, which elucidates the progress of nonanal oxidation on the WO₃ hydrate nanowire surface. Interestingly, there are several distinct differences in the oxidation and desorption behavior between the as-grown WO₃ hydrate nanowires and H₂SO₄-surface treated WO₃ hydrate nanowires. First, the temperature range where nonanoic acid is detected in the chromatograms is much lower in the case of the H₂SO₄-surface treated WO₃ hydrate nanowires (mainly at 25–75 °C), when compared to the as-grown WO₃ hydrate nanowires (mainly at 250–350 °C) (Fig. 2c). Nonanal is almost fully converted into nonanoic acid below 50 °C on the H₂SO₄-surface treated WO₃ hydrate nanowires. It is in contrast to the case of the as-grown WO₃ hydrate nanowires, in which nonanal remains up to 175 °C (Fig. 2d). These results highlight the superior oxidative activity of the surface treated WO₃ hydrate nanowires even in a low temperature range. Second, in the high temperature range (200–350 °C), some olefins and ketones (Fig. S8†) are desorbed only from the as-grown WO₃ hydrate

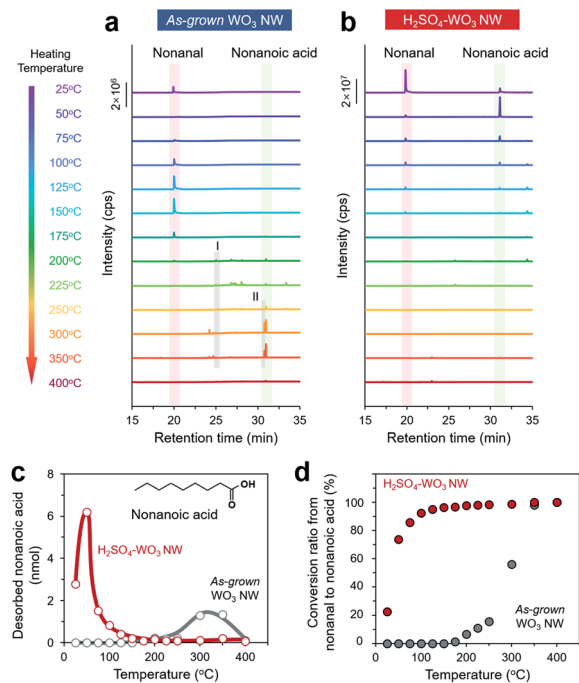


Fig. 2 (a and b) TPD-GCMS spectra of desorbed molecules from the as-grown WO₃ hydrate nanowire surfaces and H₂SO₄-treated WO₃ hydrate nanowire surfaces when elevating the temperature from 25 to 400 °C. The desorption products from the as-grown WO₃ hydrate nanowires at retention times of 25.0 min and 30.8 min correspond to 8-heptadecene (I) and 9-heptadecanone (II), respectively. (c) Calculated concentration data of desorbed nonanoic acid (nmol) from the as-grown WO₃ hydrate nanowire surfaces and H₂SO₄-treated WO₃ hydrate nanowire surfaces. The nonanoic acid calibration curve is shown in Fig. S9† (d) Comparison between the as-grown WO₃ hydrate nanowires and H₂SO₄-surface treated WO₃ hydrate nanowires regarding conversion ratio from nonanal to nonanoic acid as a function of temperature.

nanowires. These compounds are considered to be formed by the thermal decomposition of nonanoic acid,^{41,42} which remains adsorbed even in such a high temperature range. These results highlight that the adsorption of the molecules is much stronger on the as-grown WO₃ hydrate nanowires than that on the surface treated WO₃ hydrate nanowires. These trends of desorbed chemical species give information about surface chemical events related to the electrical sensor responses in Fig. 1 *i.e.*, (1) the superior catalytic characteristics of the surface treated WO₃ hydrate nanowires improves the sensing characteristics and (2) the residual compounds on the as-grown WO₃ hydrate nanowire surface lengthen the recovery time even at higher temperatures.

Although the above TPD-GCMS data identify the desorbed chemical compounds related to surface chemical reactions, they do not provide direct information on chemical events on sensor surfaces. Thus, we performed Fourier transform infrared (FT-IR) spectroscopy measurements on the sensor surface to reveal more directly surface molecular transformation behavior under sensing environments. Fig. 3a and b show the comparison between the as-grown WO₃ hydrate nanowires and H₂SO₄-

surface treated WO₃ hydrate nanowires with respect to the temperature dependent FT-IR spectra in the temperature range from 25 to 400 °C under atmospheric environments. Clearly, there are several distinct differences between the two spectra.

First, the difference of the two peaks (ν_1 and ν_2) in the 1660–1740 cm⁻¹ region reveals two distinct adsorption states of carbonyl groups, which depends on the surface acid treatment. The two peaks (ν_1 : 1710 cm⁻¹ and ν_2 : 1668 cm⁻¹) can be associated with the $\nu(\text{C}=\text{O})$ vibration mode.⁴³ Compared to the FT-IR spectrum of liquid-phase nonanal ($\nu(\text{C}=\text{O})$: 1726 cm⁻¹),⁴⁰ both $\nu_1(\text{C}=\text{O})$ and $\nu_2(\text{C}=\text{O})$ show clear red shifts, implying decreases of C–O bond orders *via* Lewis acid activation.^{40,44} Our previous work also revealed that nonanal adsorbed on the surface –OH of a metal oxide (ZnO) shows adsorption at 1709 cm⁻¹.⁴⁰ Thus, we assigned $\nu_1(\text{C}=\text{O})$ to nonanal adsorbed *via* hydrogen bonding with a surface –OH. On the other hand, the much larger red shift of $\nu_2(\text{C}=\text{O})$ implies that C=O is activated by stronger Lewis acids. Therefore, we assigned $\nu_2(\text{C}=\text{O})$ to nonanal adsorbed by coordination to a surface exposed W⁶⁺ (Fig. 3c). A theoretical calculation based on density functional theory (DFT) also supports this assignment (Fig. S10†). The wavenumber of a simplified structure of W⁶⁺-coordinated nonanal is calculated to be 1658–1688 cm⁻¹, which is in good agreement with the experimental value (1668 cm⁻¹). Based on these peak assignments, we discuss the effect of surface acid treatment on the $\nu_1(\text{C}=\text{O})$ and $\nu_2(\text{C}=\text{O})$ peaks. As can be seen in Fig. 3, at 25 °C, the as-grown WO₃ hydrate nanowires showed only the $\nu_1(\text{C}=\text{O})$ peak, whereas the H₂SO₄-surface treated WO₃ hydrate nanowires exhibited only the $\nu_2(\text{C}=\text{O})$ peak. This distinct difference can be reasonably interpreted in terms of the above assignments of the $\nu_1(\text{C}=\text{O})$ and $\nu_2(\text{C}=\text{O})$ peaks on the surface molecular structures. On the H₂SO₄-treated WO₃ hydrate nanowire surfaces, stronger Lewis acid sites (bare surface W) exist which show the $\nu_2(\text{C}=\text{O})$ peak, whereas for the as-grown WO₃ hydrate nanowires, the –OH terminated surface exhibits the $\nu_1(\text{C}=\text{O})$ peak. Thus, these results highlight that two distinct adsorption states of carbonyl groups exist, which strongly depends on the history of surface acid treatment on WO₃ hydrate nanowires.

Second, the broad peak in the 1550–1600 cm⁻¹ region in Fig. 3, which appeared only for the surface treated WO₃ hydrate nanowires, reveals the presence of carboxylate compounds on the WO₃ hydrate nanowire surface.^{38,45} Previous studies have identified that the broad peak in the 1550–1600 cm⁻¹ region corresponds to an asymmetric stretching vibration mode: $\nu_{\text{as}}(\text{COO})$ of carboxylate compounds, which are strongly bound to solid surfaces.^{46,47} This peak was not observable for the as-grown WO₃ hydrate nanowires at all. In other words, such carboxylate compounds only exist on the H₂SO₄ treated WO₃ hydrate nanowire surface. To further confirm the effect of H₂SO₄ treatment on the appearance of surface carboxylate compounds, we measured the dependence of FT-IR spectra on H₂SO₄ treatment time, as shown in Fig. 3d. As can be seen, the peak intensity in the 1550–1600 cm⁻¹ region tended to increase with the H₂SO₄ treatment time, revealing the significant effect of surface acid treatment on the appearance of surface carboxylate compounds. This can also be demonstrated by the time-

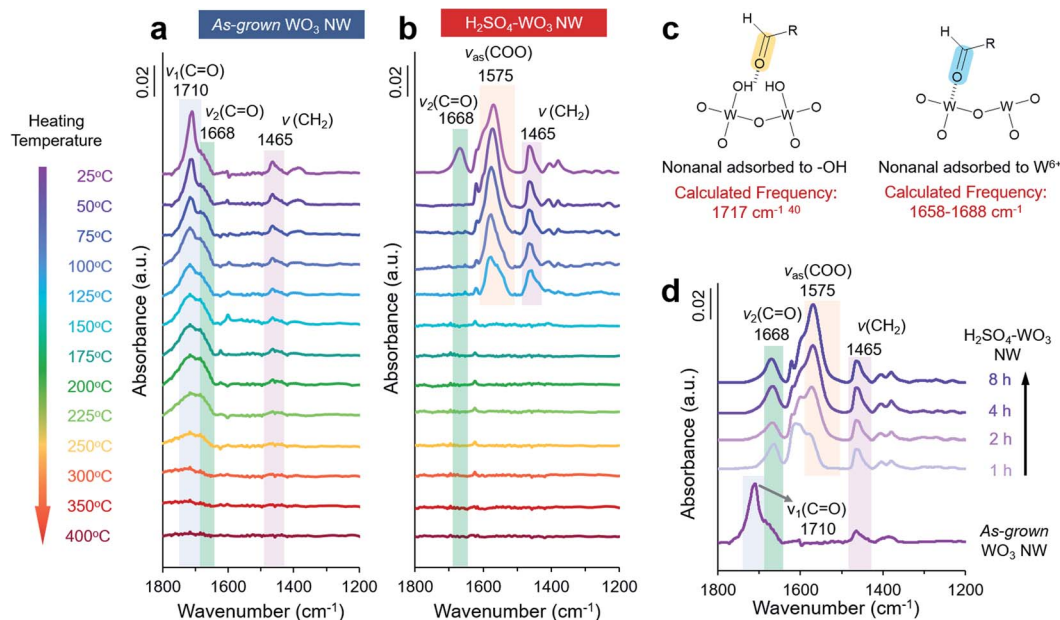


Fig. 3 (a and b) FT-IR spectra of nonanal adsorption on the as-grown WO_3 hydrate nanowires and H_2SO_4 -surface treated WO_3 hydrate nanowires when elevating the temperature from 25 to 400 °C. (c) Schematic structures of surface-adsorbed nonanal and the corresponding density functional theory (DFT)-calculated $\text{C}=\text{O}$ frequencies (see the ESI for details on the theoretical calculations†). (d) FT-IR spectra of nonanal adsorption on WO_3 hydrate nanowires for different treatment times with H_2SO_4 .

dependent FT-IR measurement (Fig. S11†). In addition, as seen in Fig. 3b, the surface carboxylate compounds desorbed at relatively low temperatures below 125 °C, which is consistent with the desorption profile of nonanoic acid for the surface treated WO_3 hydrate nanowires in Fig. 2c. On the other hand, in Fig. 3b, the $\nu_1(\text{C}=\text{O})$ peak for the as-grown WO_3 hydrate nanowires remains even at higher temperatures up to 350 °C. These temperature dependences of carbonyl groups and carboxylate compounds observed in the spectroscopic data are in good agreement with TPD-GCMS data in Fig. 2, revealing the detailed molecular transformation behavior on the WO_3 hydrate nanowire surface during the desorption process.

The above mass-spectrometric and spectroscopic results explain the effect of surface acid treatment on the molecular sensing properties (Fig. 1) in terms of the surface molecular transformation behavior on the WO_3 hydrate nanowire surface. However, we still cannot answer the following simple question: what surface structures are created by H_2SO_4 treatment, which improve the catalytic characteristics? To identify the mechanisms of catalytic surface structures, first we focus on the surface conditions before nonanal adsorption. It is noted that the spectroscopic data in Fig. 3 do not contain any experimental trends as to water molecules on the sensor surface. This is because their spectra are intentionally subtracted using a spectrum of the sample before nonanal adsorption to exclude background moisture effects on the spectra. Fig. 4a–d show the raw FT-IR spectra of the as-grown WO_3 hydrate nanowires and H_2SO_4 -surface treated WO_3 hydrate nanowires before nonanal adsorption. The annealing temperature effects on the spectra are also shown in Fig. 4a–d, since sensing experiments were performed at elevated temperatures up to 300 °C. As can be

seen, there are distinct peaks of water molecules, which are in the range of 3500–3700 cm^{-1} : a stretching mode of $\text{OH}-\nu_{\text{OH}}$, and 1595–1650 cm^{-1} : a bending mode of $\text{OH}-\delta_{\text{OH}}$.⁴³ Clearly, increasing the annealing temperature decreases the amount of water, and the H_2SO_4 treatment further enhances the removal of water from solid samples due to a strong hydration effect on SO_4^{2-} .^{48,49} Thus, there is a difference of water content between the as-grown WO_3 hydrate nanowires and H_2SO_4 -surface treated WO_3 hydrate nanowires. In addition, at elevated temperatures of sensing conditions, water related peaks almost disappeared for the H_2SO_4 -surface treated WO_3 hydrate nanowires, but not for the as-grown WO_3 hydrate nanowires. In the 1595–1650 cm^{-1} region, there are two distinct peaks of δ_{OH} . The peak at 1595–1600 cm^{-1} is associated with δ_{OH} of $\text{WO}_3 \cdot 2\text{H}_2\text{O}$, and the peak at 1620–1625 cm^{-1} can be assigned to δ_{OH} of $\text{WO}_3 \cdot \text{H}_2\text{O}$.⁵⁰ XRD measurements of these samples also show the presence of tungsten trioxide hydrates ($\text{WO}_3 \cdot x\text{H}_2\text{O}$) (Fig. S12–S14†) and the dehydration behavior when annealing (Fig. S15†) and acid treatment were performed, as shown in Fig. 4e. Thus, the results in Fig. 4a–e consistently indicate that H_2SO_4 surface treatment dehydrates WO_3 hydrate nanowires more than the as-grown WO_3 hydrate nanowires in an elevated temperature range of sensing conditions. This difference of water content in WO_3 hydrate nanowires might affect the absorption and desorption behavior. Therefore, the first possible model is based on the presence of water molecules near surfaces. This is because the presence of water near surfaces might hinder the interaction between a carbonyl group and a Lewis acid site of surface W. As seen in the spectra of Fig. 4a–d, the thermal annealing alters the water content of WO_3 hydrate nanowires. Therefore, we can examine the effect of water content on the molecular

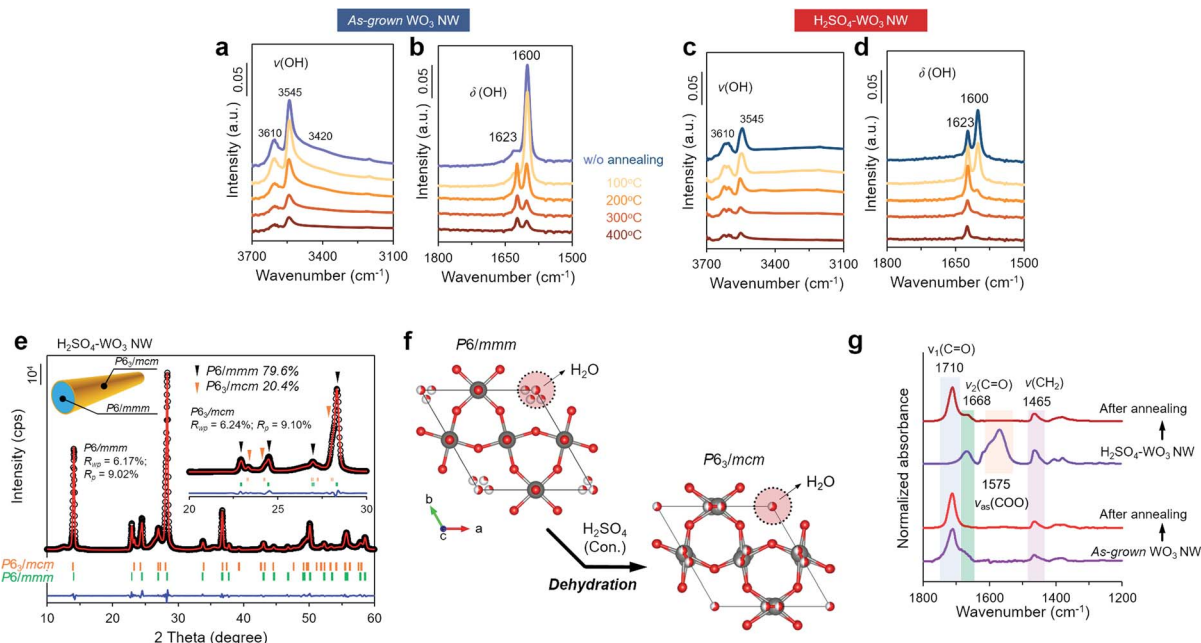


Fig. 4 (a–d) FT-IR spectra of the as-grown WO_3 nanowires and H_2SO_4 -surface treated WO_3 nanowires after thermal treatment at different temperatures. (e) X-ray diffraction (XRD) pattern and the Rietveld refinement of H_2SO_4 -surface treated WO_3 nanowires. (f) Refined crystal structure unit of the as-grown WO_3 hydrates and H_2SO_4 -surface treated WO_3 hydrates, where the red sectors in water “dots” represent the probability of water’s presence at the corresponding sites (other viewpoints are shown in Fig. S13†). (g) FT-IR spectra of nonanal adsorbed on the 400 °C annealed as-grown WO_3 nanowires and H_2SO_4 -surface treated WO_3 nanowires.

transformation behavior by using such annealed WO_3 hydrate nanowires. If the water content of WO_3 hydrate nanowires solely dominates the surface molecular transformation behavior of nonanal, the annealed WO_3 hydrate nanowires, which are dehydrated, should exhibit catalytic and molecular behavior similar to the H_2SO_4 -surface treated samples. Fig. 4g shows the spectra of nonanal adsorption on the annealed WO_3 hydrate nanowires. Contrary to our above speculation, the spectra are similar to those of the as-grown WO_3 hydrate nanowires. As shown in ESI data (Fig. S16†), the electrical sensing response of the annealed WO_3 hydrate nanowires is also similar to that of the as-grown WO_3 hydrate nanowires in terms of the recovery time, although the electrical responses are enhanced. Thus, the difference of water content in WO_3 hydrate nanowires alone cannot explain the occurrence of enhanced catalytic characteristics caused by surface acid treatment.

Here, we focus on the observed difference between surface acid treatment and thermal annealing on the dehydration process of WO_3 hydrate nanowires to clarify the mechanisms of surface acid treatment. Thermal annealing physically removes water from a solid at elevated temperatures, whereas surface acid treatment chemically dehydrates WO_3 hydrate nanowires at relatively low temperatures by utilizing the strong hydration effect on SO_4^{2-} .^{48,49} It is easily inferred that a high temperature operation of the thermal annealing process creates a thermodynamically stable solid surface structure, while a low temperature operation of chemical surface acid treatment might produce thermodynamically unstable solid surface structures.^{51,52} Extended X-ray absorption fine structure (EXAFS) analysis of the coordination structure of W can reveal such

a surface solid structure difference.^{53–55} Fig. 5a shows the normalized W L_3 -edge X-ray absorption near edge structure (XANES) of the WO_3 hydrate nanowire samples after H_2SO_4 surface treatment and thermal annealing treatment (400 °C). It can be seen that the peaks of all WO_3 hydrate nanowires are consistent with those of the standard WO_3 (10 218.5 eV), indicating that the oxidation states of W of the treated WO_3 hydrate nanowire samples do not change. This is also supported by the XPS characterization (ESI, Fig. S17†). Furthermore, the Fourier transform (FT) $k^3\chi(k)$ spectra of the WO_3 nanowire samples exhibit a dominant peak centered at 1.40 Å assignable to the W–O bond, and the W–W bond peak is centered at 3.60 Å (Fig. 5b). In addition, the FT spectra of the surface treated WO_3 hydrate nanowires showed that the W–W peaks undergo a downshift to 3.53 Å compared to those of the as-grown WO_3 hydrate nanowires, indicating that lattice contraction occurred due to the dehydration effect. Fig. 5c shows the averaged coordination number data of the first shell of a W ion from the fitting of FT $k^3\chi(k)$ spectra. The analyzed coordination number of W tends to decrease as the H_2SO_4 surface treatment time increases, while the annealing treatment has negligible effects on the coordination number of W. These results reveal the presence of coordinatively unsaturated W for the H_2SO_4 surface treated WO_3 hydrate nanowires, but not for the thermally annealed WO_3 hydrate nanowires. Thus, all the above spectroscopic results highlight that the presence of coordinatively unsaturated W of WO_3 hydrate nanowires plays an essential role in promoting the catalytic effects and molecular sensing properties shown in Fig. 1.

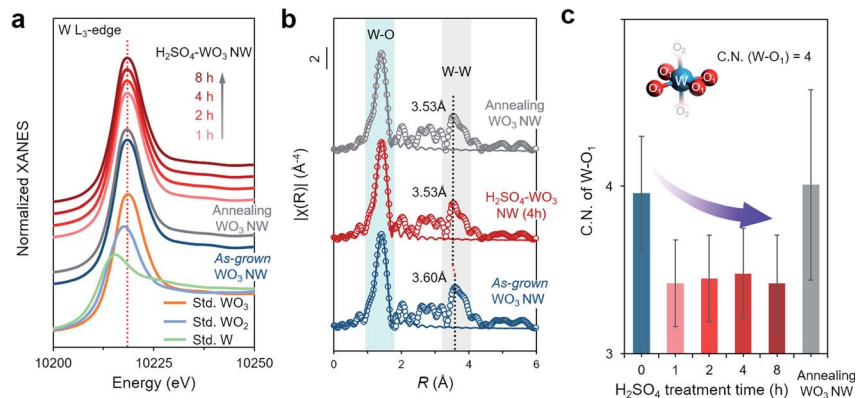


Fig. 5 (a) Normalized W L₃-edge XANES spectra of WO₃ hydrate nanowires and the standard W, WO₂ and WO₃ (Sigma Aldrich) as references. (b) Fourier transformed k^3 -weighted $\chi(k)$ -function of the EXAFS spectra (circles) and first-shell fittings (line) of WO₃ hydrate nanowires. The detailed fitting processes are shown in the ESI.† (c) W coordination numbers (C.N.) of the first shell extracted from Fourier transformed EXAFS curve fitting.

Finally, we examine the thermal durability of the surface-treated WO₃ hydrate nanowire catalysts. Fig. 6a shows the thermal durability (air-annealing temperature dependence) data from the IR spectra of the H₂SO₄ surface treated WO₃ hydrate nanowires under the sensing environment – atmospheric air – and temperature range. The air-annealing time is 1 hour. Fig. 6b shows the extracted thermal durability data of the $\nu_{\text{as}}(\text{COO})$ peak as an index of catalytic properties (oxidization of nonanal) of WO₃ hydrate nanowires. The data are shown as the ratio of the $\nu_{\text{as}}(\text{COO})$ peak at the annealing temperature to that at 25 °C. As can be seen, the catalytic properties due to acid surface treatments can be maintained up to an annealing

temperature of 300 °C, which is robust enough for electrical sensing. To further examine the robustness as a time series, Fig. 6c shows the time series data of the ratio of $\nu_{\text{as}}(\text{COO})$ peaks during durability tests for various annealing temperatures. The data are shown as the ratio of the $\nu_{\text{as}}(\text{COO})$ peak at the annealing time to that at 10 minus annealing time. For the temperature range for molecular sensing experiments around 200 °C (Fig. 1), the catalytic effect can be maintained at least over 10 years. Even at a higher temperature up to 300 °C, the catalytic activity remains over a year. Considering the surface catalytic mechanisms discussed in previous sections, this observed thermal robustness of tailored catalytic surfaces

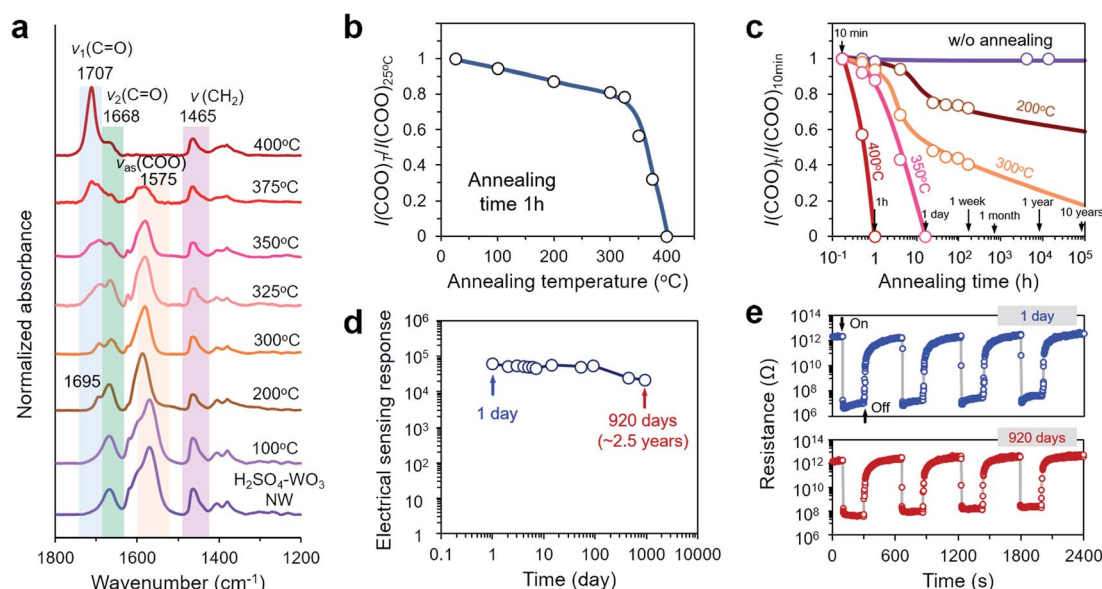


Fig. 6 (a) Temperature dependence of FT-IR spectra of H₂SO₄ surface treated WO₃ hydrate nanowire catalysis. The annealing time is 1 hour. (b) Temperature dependence of the ratio between the intensity of $\nu_{\text{as}}(\text{COO})$ after annealing ($I(\text{COO})_T$) and without annealing ($I(\text{COO})_{25^\circ\text{C}}$), which are extracted from data from (a). (c) Time series data of catalyst degradation when varying the temperature ($I(\text{COO})_t$, intensity of $\nu_{\text{as}}(\text{COO})$ after annealing for a designated time; $I(\text{COO})_{10\text{min}}$, intensity of $\nu_{\text{as}}(\text{COO})$ after annealing for 10 minutes). The raw data of FT-IR are shown in the ESI (Fig. S19 and S20).† (d) Long-term stability of the H₂SO₄ surface treated WO₃ hydrate nanowire sensor device (working at 200 °C, nonanal, 2.67 ppm. ESI Fig. S21†). (e) Dynamic resistance response of the H₂SO₄ surface treated WO₃ hydrate nanowire sensor device after storing in air for 1 day and 920 days.

corresponds to the thermal stability of coordinatively unsaturated W of WO_3 hydrate nanowires. In addition, we examine the long-term stability of H_2SO_4 surface treated WO_3 hydrate nanowire sensors for nonanal, as shown in Fig. 6d and e. As can be seen, the electrical sensing response can be maintained over 2.5 years with keeping the electrical sensitivity (4 orders of magnitude change). This long-term stable sensing data are well consistent with the catalytic activity data in Fig. 6c. Thus, these time series data quantitatively show the thermal robustness of the surface-treated WO_3 hydrate nanowire catalysis for years under sensing environments.

Conclusions

In summary, we show that a simple surface treatment using strong acids enhances both the thermally robust catalysis and electrical molecular sensing of WO_3 hydrate nanowires for carbonyl compounds. Mass-spectrometric measurements reveal that the surface treatment using strong acids substantially promotes both the oxidization of nonanal and the desorption of products, nonanoic acid, from the surfaces. Spectroscopic and structural measurements combined with numerical simulations identify two different adsorption structures of carbonyl groups on the surface, where the molecules directly bound to coordinatively unsaturated surface tungsten preferentially proceed to the catalytic oxidization reaction and the subsequent desorption process. Furthermore, we confirm the thermal durability (over 10 years) of the catalytic activity on acid-treated WO_3 hydrate nanowire surfaces up to $300\text{ }^\circ\text{C}$, which enables us to demonstrate the long-term stable sensor operations with the sensitivity (4 orders of magnitude) remaining for years. Thus, the present approach will support a better understanding and tailoring of complex nanostructured metal oxide surfaces for further sophisticated thermally robust electrical molecular sensing using heterogeneous catalysis.

Experimental

Fabrication of WO_3 hydrate nanowires

WO_3 hydrate nanowires were fabricated in two steps, which include the polytungstic acid sol synthesis and the nanowire growth.⁵⁶ For the polytungstic acid (H_2WO_4) sol synthesis, tungsten powder (4 g) (Sigma-Aldrich, 99.9%) was dissolved in hydrogen peroxide solution (H_2O_2 , 30 wt% in H_2O) (FUJIFILM Wako Pure Chemical Corp., 30.0–35.5%) in an ice bath under continuous stirring. When the W powder was dissolved, Pt foil was added to the solution to catalytically remove the unreacted H_2O_2 . As no bubbles were generated, the concentration of the as-synthesized W precursor solution was controlled using deionized (DI) water. Afterward, 50 mL of the W precursor (10.88 mM) was transferred to a 100 mL Teflon beaker. Then, 0.5625 g (6.25 mM) of oxalic acid ($\text{H}_2\text{C}_2\text{O}_4$) (Sigma-Aldrich, 99.0%) was added to the mixture and the pH was carefully controlled to 1.68 by carefully adding sodium hydroxide (NaOH, 1 M) solution. Finally, the Teflon beaker was mounted in an autoclave system and then transferred to a furnace and kept at

$200\text{ }^\circ\text{C}$ for 24 h. Finally, the WO_3 nanowires were obtained after ultracentrifugation and rinsed with DI water.

Acid and annealing treatment of WO_3 hydrate nanowires

Concentrated sulfuric acid (H_2SO_4) was utilized to dehydrate the as-grown WO_3 nanowires. The as-grown WO_3 hydrate nanowires were mixed with 50 mL of H_2SO_4 and stirred at $90\text{ }^\circ\text{C}$ for different times (1, 2, 4, and 8 h). Then, the samples were carefully rinsed with DI water to remove residual H_2SO_4 . Annealing treatment was conducted at $400\text{ }^\circ\text{C}$ in air for 1 h.

Structure characterization

Scanning electron microscopy (SEM) images were obtained using a JEOL JSM-7610F microscope. Transmission electron microscopy (TEM) images were acquired using a JEOL, JEM-ARM300F. X-ray diffraction (XRD) patterns were recorded with a Rigaku SmartLab diffractometer (Cu $K\alpha$, $\lambda = 1.5406\text{ \AA}$, 45 kV, and 200 mA). Fourier transform infrared spectroscopy (FT-IR) spectra were measured using a Nicolet iS50 FT-IR spectrometer (Thermo Fisher Scientific) equipped with an MCT detector.

Desorbed gas analysis using gas chromatography-mass spectroscopy (GC-MS)

A Shimadzu GCMS-QP 2010 Ultra instrument (equipped with a high polar InertCap FFAP capillary column and an OPTIC-4 inlet temperature control system) was used to analyze the desorbed compounds at each temperature. First, the as-grown and acid treated WO_3 nanowires (the amount of nanowires was controlled at $\sim 2\text{ mg}$) were loaded on a silicon substrate of $0.2\text{ cm} \times 2.0\text{ cm}$ size and dried at $100\text{ }^\circ\text{C}$. Nonanal liquid ($4\text{ }\mu\text{L}$) was dropped in a 25 mL closed bottle and kept for 30 min to vaporize the nonanal gas. Then, the nanowire sample was transferred into a bottle filled with nonanal gas for a fixed time (10 min) and immediately transferred into the inlet port of the GC-MS instrument for further measurements. The inlet temperature was rapidly increased ($60\text{ }^\circ\text{C s}^{-1}$) to a given temperature ($25\text{--}400\text{ }^\circ\text{C}$ with steps of $25\text{ }^\circ\text{C}$) and maintained for 10 min, then immediately cooled to $25\text{ }^\circ\text{C}$. The desorbed gas at each temperature was analyzed by mass spectroscopy. The measurements for each temperature were conducted sequentially without removing the sample from the inlet port. The detailed temperature program is shown in Fig. S6.†

FT-IR monitoring of the molecular adsorption progress

First, the as-grown and acid treated WO_3 nanowires (the amount of nanowires was controlled at $\sim 50\text{ mg}$) were loaded on a silicon substrate of $2.0\text{ cm} \times 2.0\text{ cm}$ size and dried at $100\text{ }^\circ\text{C}$. Nonanal liquid ($20\text{ }\mu\text{L}$) was dropped in a 100 mL closed bottle and kept for 30 min to vaporize the nonanal gas. Then, the sample was transferred into a bottle filled with nonanal gas for a fixed time (10 min) and immediately transferred into the FT-IR chamber for further measurements. The nonanal-adsorbed WO_3 nanowires were heated at a given temperature ($25\text{--}400\text{ }^\circ\text{C}$ with steps of $25\text{ }^\circ\text{C}$) for 10 min and cooled to room temperature. The FT-IR spectra of the nanowires were then

recorded at room temperature on a Thermo Fisher Scientific Nicolet iS50 FT-IR spectrometer equipped with an MCT detector.

X-ray absorption spectroscopy

XANES and EXAFS analyses of the W L_{3} -edge were performed in transmission mode at the BL 06 (Kyushu University beamline) of the SAGA-LS (Saga, Japan) with a storage ring operating at an energy of 1.4 GeV. A monochromator with two Si (111) crystals was used to scan the energy of the X-ray beam. The photon flux was 2×10^{10} photons per second. The intensities of the fluorescence X-rays were monitored using a silicon drift detector. Powder samples of the standard W, WO_2 , and WO_3 , and WO_3 nanowire samples were diluted with boron nitride to obtain the optimum concentration and then pressed into a tablet with a diameter of 1 cm. The spectra of the prepared pellet samples were measured in transmission mode. XANES data processing and r -space fitting of XAFS data were carried out using Athena and Artemis included in the Iffeffit package. The detailed fitting processes are shown in the ESI.†

Computational analyses of molecular vibrational infrared spectra

DFT calculations were carried out to compute the vibrational frequencies of nonanal molecules bonding on the hexagonal WO_3 (100) plane. We used a simplified cluster model to mimic the WO_3 (100) plane. The cluster model for the W^{6+} site model consisted of a single tungsten atom and five oxygen atoms. We fixed the atomic configurations of these two cluster models during the geometry optimization. We employed B3LYP-D3 as the functional. According to the comparison with the results from other functionals (ω B97XD, APFD, B3LYP, or B3LYP-D3), dependency on the used functional is found to be negligible in this calculation. A more detailed discussion is provided in the ESI.†

Fabrication of the single nanowire device and molecular sensing measurement

A nanowire suspension was prepared by mixing the fabricated nanowire samples with 2-propanol with light sonication. Then, the dispersed nanowires were transferred onto a 100 nm thick SiO_2 coated Si (100) substrate with pre-patterned contact Pt electrodes. Electron beam (EB) lithography (Elionix, ELS-S50YND) was performed at an accelerating voltage of 50 kV to make the electrode patterns for bridging a single nanowire with the contact electrodes using ZEP520A-7 (ZEON) as a resist. A 800 nm layer of Pt was then deposited by RF sputtering (SEINAN) in an Ar 0.4 Pa atmosphere. Afterward, lift-off (N,N -dimethylformamide) and acetone cleaning processes were conducted to complete the device fabrication. The gap size of bridged nanowires was designed to be 1 μ m and the nanowires with *ca.* 300–400 nm diameter were chosen for all fabricated devices to eliminate the variation of electrical properties caused by the device geometry. The sensing performance to nonanal was analyzed by using a self-made chamber combined with a Keithley 4200A-SCS Parameter Analyzer (Tektronix, Inc.).

Resistance of the WO_3 nanowire device under N_2 was recorded as baseline (R_{N_2}). The resistance upon exposure of nonanal gas (produced by bubbling liquid nonanal solution) was noted as R_{gas} , and sensing response was defined as R_{N_2}/R_{gas} . The recovery time was defined as the time required for the recovery of the resistance to 90% of R_{N_2} for the desorption process. All the sensing tests were carried out under a DC bias voltage of 1 V. Nonanal gas was produced by bubbling liquid nonanal solution with highly pure N_2 , and its concentration was calibrated using GCMS (Shimadzu GCMS-QP2010 Ultra) with a temperature control system (GL Sciences, OPTIC-4). The flow rates of dry air and the nonanal gas were controlled at 200 sccm during the sensing performance tests and the testing temperature was set to vary from 25 to 250 °C. The bubbling nonanal gas was diluted 400 times to the ppb level for the sensing test. 10–15 devices were fabricated for each sample to obtain statistical data.

Author contributions

T. Y. proposed the research direction and guided the project. G. Z., T. H., J. L., K. N. and T. Y. designed and performed the entire experiment. W. M. and T. H. carried out computational investigation and provided theoretical analysis. All authors analyzed and discussed the experimental results. T. S. performed XANES and EXAFS analyses. G. Z. and T. Y. drafted the manuscript. All the other authors participated in preparing the manuscript and contributed to the discussion.

Conflicts of interest

There are no conflicts to declare.

Acknowledgements

This work was supported by KAKENHI (18H0524) and JST-CREST (JPMJCR19I2). XANES and EXAFS analyses of the W L_{3} -edge were performed in transmission mode at the BL 06 (Kyushu University beamline) of the SAGA-LS, Saga. The computation in this work was performed using the facilities of RIIT, Kyushu University. The study was supported by the General Research Fund of the Research Grants Council of Hong Kong SAR, China (CityU 11211317).

Notes and references

- 1 A. Lewis and P. Edwards, *Nature*, 2016, **535**, 29–31.
- 2 K. Kalantar-Zadeh, K. J. Berean, N. Ha, A. F. Chrimes, K. Xu, D. Grando, J. Z. Ou, N. Pillai, J. L. Campbell, R. Brkljaca, K. M. Taylor, R. E. Burgell, C. K. Yao, S. A. Ward, C. S. McSweeney, J. G. Muir and P. R. Gibson, *Nat. Electron.*, 2018, **1**, 79–87.
- 3 K. Iitani, P. Chien, T. Suzuki, K. Toma, T. Arakawa, Y. Iwasaki and K. Mitsubayashi, *ACS Sens.*, 2018, **3**, 425–431.
- 4 V. Galstyan, N. Poli, A. D'Arco, S. Macis, S. Lupi and E. Comini, *J. Mater. Chem. A*, 2020, **8**, 20373–20385.
- 5 X. X. Wang, H. Y. Li and X. Guo, *J. Mater. Chem. A*, 2020, **8**, 14482–14490.

- 6 A. Dey, *Mater. Sci. Eng., B*, 2018, **229**, 206–217.
- 7 D. R. Miller, S. A. Akbar and P. A. Morris, *Sens. Actuators, B*, 2014, **204**, 250–272.
- 8 Q. Fu and X. Bao, *Chem. Soc. Rev.*, 2017, **46**, 1842–1874.
- 9 N. Barsan and U. Weimar, *J. Electroceram.*, 2001, **7**, 143–167.
- 10 A. Cabot, A. Dieguez, A. Romano-Rodriguez, J. Morante and N. Barsan, *Sens. Actuators, B*, 2001, **79**, 98–106.
- 11 G. Korotcenkov, *Mater. Sci. Eng., B*, 2007, **139**, 1–23.
- 12 D. P. Volanti, A. A. Felix, M. O. Orlandi, G. Whitfield, D.-J. Yang, E. Longo, H. L. Tuller and J. A. Varela, *Adv. Funct. Mater.*, 2013, **23**, 1759–1766.
- 13 H. Long, A. Harley-Trochimczyk, T. Pham, Z. Tang, T. Shi, A. Zettl, C. Carraro, M. A. Worsley and R. Maboudian, *Adv. Funct. Mater.*, 2016, **26**, 5158–5165.
- 14 X. Wang, Z. Wang, J. Zhang, X. Wang, Z. Zhang, J. Wang, Z. Zhu, Z. Li, Y. Liu, X. Hu, J. Qiu, G. Hu, B. Chen, N. Wang, Q. He, J. Chen, J. Yan, W. Zhang, T. Hasan, S. Li, H. Li, H. Zhang, Q. Wang, X. Huang and W. Huang, *Nat. Commun.*, 2018, **9**, 3611.
- 15 R. H. Crabtree, *Chem. Rev.*, 2015, **115**, 127–150.
- 16 E. D. Goodman, A. C. Johnston-Peck, E. M. Dietze, C. J. Wrasman, A. S. Hoffman, F. Abild-Pedersen, S. R. Bare, P. N. Plessow and M. Cargnello, *Nat. Catal.*, 2019, **2**, 748–755.
- 17 P. Fuchs, C. Loeseken, J. K. Schubert and W. Miekisch, *Int. J. Cancer*, 2010, **126**, 2663–2670.
- 18 A. C. Romain and J. Nicolas, *Sens. Actuators, B*, 2010, **146**, 502–506.
- 19 H. Yang, X. Bai, P. Hao, J. Tian, Y. Bo, X. Wang and H. Liu, *Sens. Actuators, B*, 2019, **280**, 34–40.
- 20 Q. Zhou, L. Xu, A. Umar, W. Chen and R. Kumar, *Sens. Actuators, B*, 2019, **256**, 656–664.
- 21 Y. Wang, P. Cheng, X. Li, C. Wang, C. Feng and G. Lu, *J. Mater. Chem. C*, 2020, **8**, 78–88.
- 22 J. E. Lee, H. K. Lee, H. J. Park, A. Ma, S. Y. Choi and D. S. Lee, *Sens. Actuators, B*, 2019, **292**, 289–296.
- 23 Q. Zhou, W. Zeng, W. Chen, L. Xu, R. Kumar and A. Umar, *Sens. Actuators, B*, 2019, **298**, 126870.
- 24 Y. Z. Chen, S. H. Lee, T. Y. Su, S. C. Wu, P. J. Chen and Y. L. Chueh, *J. Mater. Chem. A*, 2019, **7**, 22314–22322.
- 25 C. Su, L. Zhang, Y. Han, C. Ren, M. Zeng, Z. Zhou, Y. Su, N. Hu, H. Wei and Z. Yang, *Sens. Actuators, B*, 2020, **304**, 127347.
- 26 Z. Zhu, L. Zheng, S. Zheng, J. Chen, M. Liang, Y. Tian and D. Yang, *J. Mater. Chem. A*, 2018, **6**, 21419–21427.
- 27 S. Liu, S. Gao, Z. Wang, T. Fei and T. Zhang, *Sens. Actuators, B*, 2019, **290**, 493–502.
- 28 M. Al-Hashem, S. Akbar and P. Morris, *Sens. Actuators, B*, 2019, **301**, 126845.
- 29 D. Kohl, *Sens. Actuators, B*, 1990, **1**, 158–165.
- 30 G. Korotcenkov, *Sens. Actuators, B*, 2005, **107**, 209–232.
- 31 D. Degler, S. Wicker, U. Weimar and N. Barsan, *J. Phys. Chem. C*, 2015, **119**, 11792–11799.
- 32 S. Sanze, A. Gurlo and C. Hess, *Angew. Chem., Int. Ed.*, 2013, **52**, 3607–3610.
- 33 A.-K. Elger and C. Hess, *Angew. Chem., Int. Ed.*, 2019, **58**, 15057–15061.
- 34 D. Koziej, M. Hübner, N. Barsan, U. Weimar, M. Sikora and J.-D. Grunwaldt, *Phys. Chem. Chem. Phys.*, 2009, **11**, 8620–8625.
- 35 S. Müller, A. Zimina, R. Steininger, S. Flessau, J. Osswald and J. D. Grunwaldt, *ACS Sens.*, 2020, **5**, 2486–2496.
- 36 D. Degler, S. Rank, S. Müller, H. W. Pereira de Carvalho, J. Grunwaldt, U. Weimar and N. Barsan, *ACS Sens.*, 2016, **1**, 1322–1329.
- 37 S. Wicker, M. Guiltat, U. Weimar, A. Hemeryck and N. Barsan, *J. Phys. Chem. C*, 2017, **121**, 25064–25073.
- 38 A. Staerz, S. Somacescu, M. Epifani, T. Kida, U. Weimar and N. Barsan, *ACS Sens.*, 2020, **5**, 1624–1633.
- 39 T. Suzuki, A. Sackmann, A. Oprea, U. Weimar and N. Barsan, *ACS Sens.*, 2020, **5**, 2555–2562.
- 40 C. Wang, T. Hosomi, K. Nagashima, T. Takahashi, G. Zhang, M. Kanai, H. Zeng, W. Mizukami, N. Shioya, T. Shimoaka, T. Tamaoka, H. Yoshida, S. Takeda, T. Yasui, Y. Baba, Y. Aoki, J. Terao, T. Hasegawa and T. Yanagida, *Nano Lett.*, 2019, **19**, 2443–2449.
- 41 J. L. Grant, C. H. Hsieh and T. M. Makris, *J. Am. Chem. Soc.*, 2015, **137**, 4940–4943.
- 42 M. Renz, *Eur. J. Org. Chem.*, 2005, 979–988.
- 43 S. George, *Infrared and Raman Characteristic Group Frequencies: Tables and Charts*, John Wiley & Sons, 2004.
- 44 M. I. Zaki, M. A. Hasan and L. Pasupulety, *Langmuir*, 2001, **17**, 768–774.
- 45 P. Patrono, A. La Ginestra, G. Ramis and G. Busca, *Appl. Catal., A*, 1994, **107**, 249–266.
- 46 S. K. Papageorgiou, E. P. Kouvelos, E. P. Favvas, A. A. Sapalidis, G. E. Romanos and F. K. Katsaros, *Carbohydr. Res.*, 2010, **345**, 469–473.
- 47 X. Jia, J. Ma, F. Xia, Y. Xu, J. Gao and J. Xu, *Nat. Commun.*, 2018, **9**(1), 1–7.
- 48 B. JO'M, M. Gamboa-Aldeco and M. Szklarczyk, *J. Electroanal. Chem.*, 1992, **339**, 355–400.
- 49 X. B. Wang, A. P. Sergeeva, J. Yang, X.-P. Xing, A. I. Boldyrev and L. S. Wang, *J. Phys. Chem. A*, 2009, **113**, 5567–5576.
- 50 M. F. Daniel, B. Desbat, J. C. Lassegues, B. Gerand and M. Figlarz, *J. Solid State Chem.*, 1987, **67**, 235–247.
- 51 P. Krüger, I. Koutiri and S. Bourgeois, *Phys. Rev. B: Condens. Matter Mater. Phys.*, 2012, **86**, 224102.
- 52 D. Saha, K. M. Ø. Jensen, C. Tyrsted, E. D. Bøjesen, A. H. Mamakhel, A.-C. Dippel, M. Christensen and B. B. Iversen, *Angew. Chem., Int. Ed.*, 2014, **53**, 3667–3670.
- 53 Y. H. Li, P. F. Liu, L. F. Pan, H. F. Wang, Z. Z. Yang, L. R. Zheng, P. Hu, H. J. Zhao, L. Gu and H. G. Yang, *Nat. Commun.*, 2015, **6**, 8064.
- 54 N. Zhang, X. Li, H. Ye, S. Chen, H. Ju, D. Liu, Y. Lin, W. Ye, C. Wang, Q. Xu, J. Zhu, L. Song, J. Jiang and Y. Xiong, *J. Am. Chem. Soc.*, 2016, **138**, 8928–8935.
- 55 Y. Ren, Y. Zou, Y. Liu, X. Zhou, J. Ma, D. Zhao, G. Wei, Y. Ai, S. Xi and Y. Deng, *Nat. Mater.*, 2020, **19**, 203–211.
- 56 G. Zhang, C. Wang, W. Mizukami, T. Hosomi, K. Nagashima, H. Yoshida, K. Nakamura, T. Takahashi, M. Kanani, T. Yasui, Y. Aoki, Y. Baba and T. Yanagida, *Nanoscale*, 2020, **12**, 9058–9066.